Check for updates

JGR Atmospheres

RESEARCH ARTICLE
10.1029/2025JD043909

Transitions Toward a Midheavy State of Tropical Convection

Hirohiko Masunaga[1] **and Hanii Takahashi**[2]

[1]Institute for Space-Earth Environmental Research, Nagoya University, Nagoya, Japan, [2]Jet Propulsion Laboratory, California Institute of Technology, Pasadena, CA, USA

Key Points:

- Satellite observations of precipitation and radiation are analyzed to diagnose the vertical motion effects on tropical convective evolution
- Hourly changes of precipitation and atmospheric cloud radiative effect have a tendency of converging toward a certain intermediate value
- This value finds itself in a dynamically stable state maintained with a midheavy vertical profile of vertical motion

Correspondence to:
H. Masunaga,
masunaga@nagoya-u.jp

Citation:
Masunaga, H., & Takahashi, H. (2025). Transitions toward a midheavy state of tropical convection. *Journal of Geophysical Research: Atmospheres*, *130*, e2025JD043909. https://doi.org/10.1029/2025JD043909

Received 19 MAR 2025
Accepted 15 NOV 2025

Abstract This study analyzes the thermodynamic effects of atmospheric vertical motion recorded in satellite observations to investigate the processes behind the evolution of tropical convection. These processes, difficult to observe directly, are diagnosed from satellite retrievals of precipitation (P) and atmospheric cloud radiative effect (ACRE) with the aid of a simple theory. It is found that hourly changes of P and ACRE projected onto the P-ACRE plane have a tendency of pointing toward a settling point at LP $\sim$ 700 W m^{-2} and ACRE $\sim$ 75 W m^{-2}, corresponding to a state of midheavy ascent. These physically driven transitions are counteracted largely by inverse transitions ascribed mainly to the stochastic effects due to a sample density gradient, except where samples are very few. The net effect of these mutually competing transitions is an evolutionary path qualitatively reminiscent of the known Lagrangian life cycle of a traveling convective system, whereas the P-ACRE trajectory stays in the close vicinity of the settling point when spatially averaged over the system.

Plain Language Summary The tropical atmosphere tends to get wetter or drier when an upward or downward motion of air occurs, and this effect helps raining clouds grow deep or die out depending on how high the air motion reaches up. Understanding how the vertical air motion shapes itself is thus a key to better predict tropical weather. Since the vertical air motion is difficult to estimate from observations, this study instead analyzes precipitation and atmospheric radiation available from satellite data as a convenient measure of how deep the upward air motion is extended. Observations reveal two contrasting states of the upward motion that are confined to near-surface motion and peaked at upper levels, each having a tendency of jumping to a state in between. This result sheds light on a previously unknown aspect of the mechanism how tropical weather is driven and maintained.

1. Introduction

The influence of Earth's rotation on atmospheric dynamics is so limited at low latitudes that tropical moist convection is governed by the intricate interplay across scales between atmospheric motion and local thermodynamic forcing. This contrasts with the dynamics of midlatitude disturbances, which are shaped on a synoptic scale under tight control of quasi-geostrophic balance. An ensemble of tropical convective clouds is instead linked with the domain-mean vertical motion in such a way as the net diabatic heating is nearly balanced against the adiabatic cooling of ascending air under the weak temperature gradient (WTG) approximation (Charney, 1963; Sobel et al., 2001). The WTG approximation is useful for simplifying the theoretical formulation of convective dynamics while not necessarily helpful per se for deciphering the processes at work behind it.

The variability of low- and midtropospheric moisture is a key factor promoting or suppressing convective activities (e.g., Bretherton et al., 2004; Holloway & Neelin, 2009; Sherwood, 1999; Yoneyama & Fujitani, 1995). The tropospheric moisture budget is a central element in theories of tropical convection as well as the thermal energy conservation assuring the WTG balance. The thermal balance equation may be replaced by the moist static energy (MSE) budget equation when MSE conservation is deemed more intuitively useful. For example, the MSE budget is practical for evaluating the effects of vertical motion on column-integrated thermodynamic properties, or in short, the column processes (Chikira, 2014).

The column processes of moisture and MSE change in sign and magnitude depending on the vertical structure of vertical motion (Figure 1). A vertical motion profile is called bottom-heavy motion when the ascent is confined to the lower troposphere, while it is referred to as top-heavy motion when the updraft peak is at a higher level near the tropopause. A bottom-heavy ascent leads to an import of moisture and MSE into the column for a typical tropical sounding, while MSE is exported out of the column as the upward motion extends toward higher levels

© 2025. The Author(s).
This is an open access article under the terms of the Creative Commons Attribution License, which permits use, distribution and reproduction in any medium, provided the original work is properly cited.

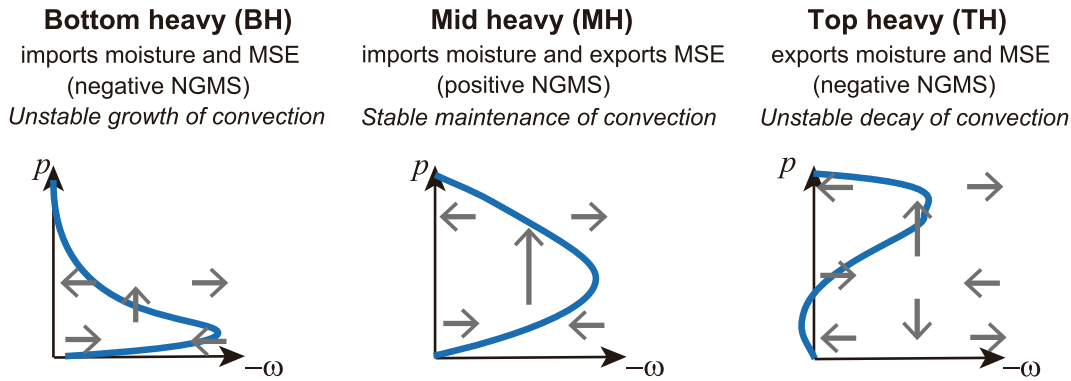

Figure 1. Bottom-heavy, midheavy, and top-heavy vertical motion and their consequences on column-integrated moisture and moist static energy.

(Inoue & Back, 2015b). Convection is hence allowed to grow on its own in a bottom-heavy ascent but is sustained in a stable manner for an updraft having a midtropospheric peak, as long as moisture is imported into the column. This category of vertical motion is hereafter called a midheavy ascent, in distinction from a top-heavy ascent with an upper-tropospheric peak accompanying a low-level divergence. A top-heavy ascent defined in this way would export both moisture and MSE and thus result in a dissipation of convection. Such contrasting behaviors depending on the top-heaviness of vertical motion may be summarized qualitatively by the normalized gross moist stability (NGMS), defined as the ratio of the column import of MSE to that of moisture (Raymond et al., 2007). Moist convection is stably maintained when NGMS is positive, while otherwise subject to an unstable growth or dissipation (Raymond et al., 2009).

The evolution from bottom-heavy to top-heavy vertical motion is characteristic of tropical disturbances across a broad range of temporal scales, with the shortest being several hours as typical of the lifetime of organized convective systems (Mapes et al., 2006). The column-process thinking has served as a useful conceptual tool in a series of studies looking into the development and maintenance of tropical convection with focus on global and regional climatology (Back & Bretherton, 2009; Back et al., 2017; Inoue et al., 2021; Masunaga, 2023), large-scale transients (Inoue et al., 2020; Kuang, 2011), and convective life cycle (Masunaga & L'Ecuyer, 2014; Maithel & Back, 2022; Masunaga & Takahashi, 2024).

Masunaga and Takahashi (2024), hereafter MT24 devised an analysis method to diagnose the top-heaviness of vertical motion with satellite observables and tested it against satellite-tracked convective life cycle. Their results were somewhat unexpected in some aspects. The Lagrangian life cycle of convective systems as a whole was found not to follow a monotonic progression from bottom-heavy to top-heavy states but instead stays nearly in a dynamic equilibrium among diverse internal states with different degrees of top-heaviness. While physical processes explaining such two-way transitions embedded in the convective system evolution are yet to be fully understood, MT24's finding suggests a pathway to reconcile contrasting perspectives to understand the evolution of convection, that is, one from the cloud-system point of view (e.g., convective life cycle) and the other based on large-scale moist convective dynamics (e.g., vertical motion and NGMS).

Motivated to address this outstanding question, this study analyzes satellite-retrieved precipitation (P) and atmospheric cloud radiative effect (ACRE) or difference between all-sky and clear-sky column-integrated radiative heating rates, to investigate hour-to-hour variability in the column processes. P and ACRE are chosen because the column import/export of moisture and MSE is derived semianalytically as a function of these two observables in the conceptual model of MT24. To see how P and ACRE evolve over time, temporal changes of P and ACRE are projected onto the P-ACRE plane in expectation that trajectories representing convective lifecycle would emerge themselves. As will be shown later, the resulting trajectories turn out to be comprised unexpectedly of transitions converging toward a certain point. This contrasts with thermodynamic diagrams of convective evolution often circling in a closed circuit (Igel, 2017; Inoue & Back, 2017; Wolding et al., 2022) but resembles a diverging/converging vector field as found by Wolding et al. (2020) despite the difference in time scale of interest. This article is aimed at exploring a possible interpretation of this seemingly unintuitive observational evidence from thermodynamic and statistical perspectives.

21698996, 2025, 23, Downloaded from https://agupubs.onlinelibrary.wiley.com/doi/10.1029/2025JD043909 by Hirohiko Masunaga - MPI 348 Meteorology , Wiley Online Library on [01/12/2025]. See the Terms and Conditions (https://onlinelibrary.wiley.com/terms-and-conditions) on Wiley Online Library for rules of use; OA articles are governed by the applicable Creative Commons License

21698996, 2025, 23, Downloaded from https://agupubs.onlinelibrary.wiley.com/doi/10.1029/2025JD043909 by Hirohiko Masunaga - MPI 348 Meteorology , Wiley Online Library on [01/12/2025]. See the Terms and Conditions (https://onlinelibrary.wiley.com/terms-and-conditions) on Wiley Online Library for rules of use; OA articles are governed by the applicable Creative Commons License

2. Data and Method

The current analysis necessitates observations of P and ACRE with a dense (hourly) temporal sampling covering the global tropics. To meet this requirement, P and ACRE are taken from the Integrated Multi-satellitE Retrievals for Global Precipitation Measurement (IMERG) V06 data set (Huffman et al., 2020) and the Clouds and the Earth's Radiant Energy System (CERES) Synoptic 1° (SYN1deg) data product (Doelling et al., 2016), respectively. ACRE is calculated from the all-sky and (hypothetical) clear-sky radiative fluxes, each provided by the CERES SYN1deg product. The half-hourly, 0.1° × 0.1°-gridded IMERG data are adjusted to an hourly, 1° × 1° grid to match the resolution native to the SYN1deg data. All longitudes bound between the latitudes of 25°S and 25°N for two years—2007 and 2008—are analyzed. Singling out either ocean or land surfaces or narrowing the latitudinal range has been confirmed not to qualitatively change the present results.

Three convective regimes, namely the bottom-heavy (BH), midheavy (MH), and top-heavy (TH) regimes, are defined with P and ACRE following MT24's procedures as summarized below. The column-integrated moisture and MSE budget equations as differentiated between all-sky and clear-sky conditions are

$$D_t\langle q\rangle' + \langle \omega \partial_p q\rangle' \approx -P, \tag{1}$$

$$D_t\langle h\rangle' + \langle \omega \partial_p h\rangle' \approx \langle Q_R\rangle', \tag{2}$$

where $D_t \equiv \partial_t + \mathbf{v}_H \cdot \nabla_H$ is the Lagrangian derivative operator, q is the water vapor mixing ratio, h is MSE per unit mass, p is pressure, ω is vertical p velocity, P is precipitation, Q_R is the net radiative heating, and $\langle \cdots \rangle$ signifies the vertical integral over the depth of the atmosphere. The excess or deficit of an all-sky value against its clear-sky counterpart is denoted by prime symbols, so $\langle Q_R\rangle'$ refers to ACRE by definition (in this paper, ACRE always refers to the net ACRE with its shortwave and longwave components combined). Note that surface evaporation flux and sensible heat flux do not appear in Equations 1 and 2 owing to the assumption that these turbulent heat fluxes are by far less sensitive to cloudiness than P and $\langle Q_R\rangle'$. The variability in latent and sensible heat fluxes, although likely modulated to some degree during a passage of individual rainfall events, is largely smoothed out when many events are averaged together (Masunaga, 2013).

The vertical structure of ω is expanded into a series of baroclinic modes with different vertical wavelengths, among which only the lowest two modes are considered in this analysis. The first and second modes are characterized in the current formulation by two prescribed parameters of γ_i and η_i, where the subscript i denotes the mode number ($i = 1$ and 2). The first parameter, γ_i, is a variant of NGMS that is defined individually for each mode as follows:

$$\gamma_i \equiv -\frac{\langle \omega_i \partial_p h\rangle'}{L\langle \omega_i \partial_p q\rangle'}, \tag{3}$$

where L is the specific latent heat. The first-mode GMS or γ_1 is positive and decreases with increasing column water vapor (CWV) while γ_2 is nearly constant at a negative value (see Figure 8b of Masunaga and Mapes (2020)). The second parameter, η_i, is the precipitation inefficiency given by

$$D_t\langle q\rangle' = -\eta_1\langle \omega_1 \partial_p q\rangle' - \eta_2\langle \omega_2 \partial_p q\rangle', \tag{4}$$

where $\eta_1 \sim 0$ and $\eta_2 \sim 1$ (Masunaga & Sumi, 2017). The specific formula of γ_i and η_i are as given by Equations 17–20 of MT24, using CWV obtained from European Centre for Medium-Range Weather Forecasts Reanalysis v5 (ERA5) (Hersbach et al., 2020) to determine γ_1. With the aid of these parameterizations and a WTG assumption of $D_t\langle h\rangle' \approx LD_t\langle q\rangle'$, Equations 1 and 2 are reduced to a pair of algebraic equations as follows:

$$L\langle \omega_1 \partial_p q\rangle' = -\frac{(\gamma_2+\eta_2)LP - (1-\eta_2)\langle Q_R\rangle'}{(\gamma_2+\eta_2)(1-\eta_1) - (\gamma_1+\eta_1)(1-\eta_2)}, \tag{5}$$

$$L\langle \omega_2 \partial_p q\rangle' = \frac{(\gamma_1+\eta_1)LP - (1-\eta_1)\langle Q_R\rangle'}{(\gamma_2+\eta_2)(1-\eta_1) - (\gamma_1+\eta_1)(1-\eta_2)}. \tag{6}$$

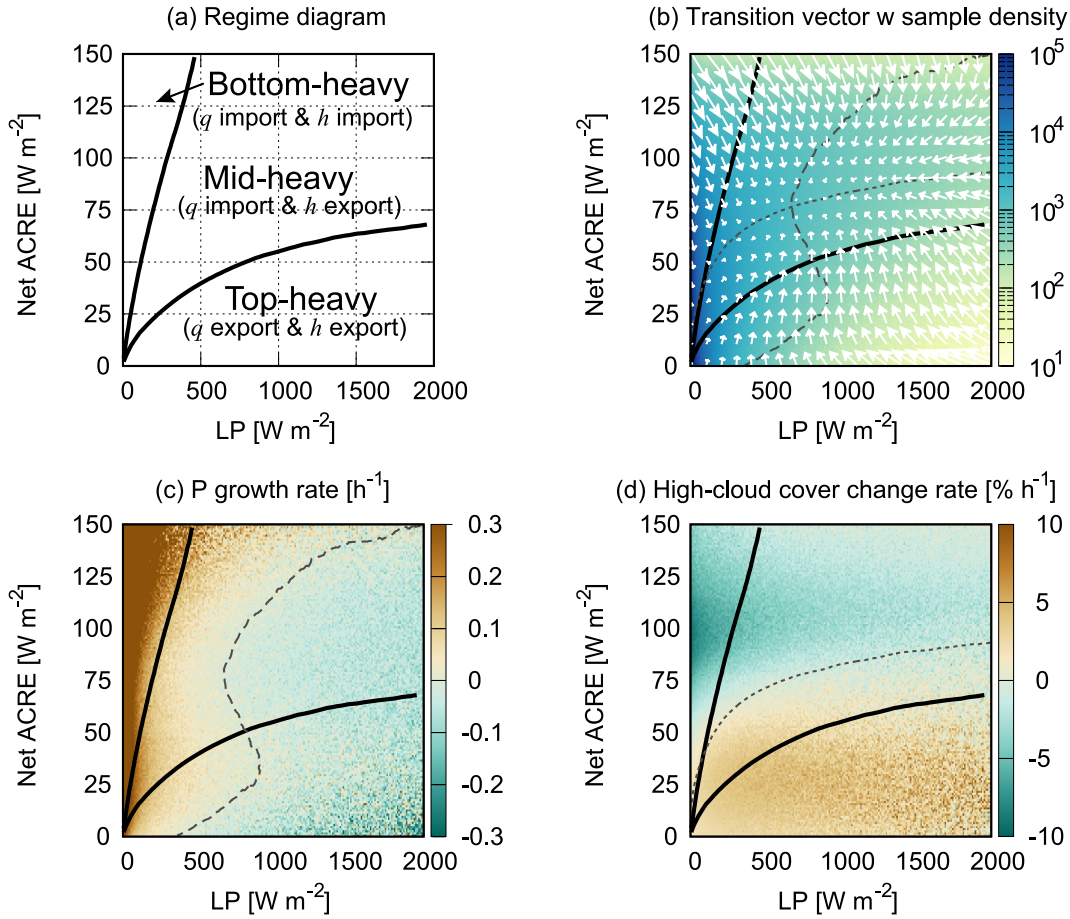

Figure 2. The *P*-ACRE diagrams of (a) convective regimes, (b) sample density (color shade) overlaid by (forward) transition vectors, (c) precipitation growth rate, and (d) the temporal change rate of high cloud cover. Thick black curves common to all panels are boundaries separating the convective regimes. Vector length implies the hourly interval of transition in (b). The zero contour of the x component of transition vectors is dashed in (b) and (c) and that of the y component is dotted in (b) and (d).

It is noted that the WTG assumption is justifiable for the spatial and temporal scales of present interest. Given that gravity waves with a typical propagation speed of 50 m s^{-1} travel over a distance of about 1.6° for 1 hour, temperature perturbations are considered to have been (barely) smoothed out in hourly, 1° × 1° data. Care must be taken when the assumption of zero temperature tendency is applied to individual events for which a diurnally induced temperature perturbation is non-negligible. This effect is minor when all samples are composited together regardless of local time, because the diurnal forcing to temperature tendency is canceled out by construction when integrated over 24 hr.

The column export of moisture and MSE is evaluated from Equations 5 and 6 as follows:

$$\text{Moisture export: } \langle \omega \partial_p q \rangle' = \langle \omega_1 \partial_p q \rangle' + \langle \omega_2 \partial_p q \rangle', \tag{7}$$

$$\text{MSE export: } \langle \omega \partial_p h \rangle' = -\gamma_1 L \langle \omega_1 \partial_p q \rangle' - \gamma_2 L \langle \omega_2 \partial_p q \rangle'. \tag{8}$$

The column import simply refers to the negative column export. The convective regimes are distinguished by the direction of the moisture and MSE import/export: the BH regime is defined when moisture and MSE are both imported into the column, the TH regime when moisture and MSE are both exported out of the column, and the MH regime when moisture is imported and yet MSE is exported (Figure 1). This classification is applied to 2 years of observations over the global tropics and yields a convective regime diagram in the *P*-ACRE plane as shown in Figure 2a.

21698996, 2025, 23, Downloaded from https://agupubs.onlinelibrary.wiley.com/doi/10.1029/2025JD043909 by Hirohiko Masunaga - MPI 348 Meteorology , Wiley Online Library on [01/12/2025]. See the Terms and Conditions (https://onlinelibrary.wiley.com/terms-and-conditions) on Wiley Online Library for rules of use; OA articles are governed by the applicable Creative Commons License

3. Transition Vectors and Settling Point

First examined are transition vectors constituted of hourly changes in P and ACRE. For the convenience of computation, the P-ACRE plane is discretized into small two-dimensional bins so that any given pair of P and ACRE are approximated by the bin in which they fall. When P and ACRE change from the i-th to j-th bins over a time interval of Δt, the (instantaneous) transition vector is

$$\mathbf{v}_{i\to j} = \begin{pmatrix} (LP_j - LP_i)/\Delta t \\ (\mathrm{ACRE}_j - \mathrm{ACRE}_i)/\Delta t \end{pmatrix}, \tag{9}$$

where LP denotes P in energy flux units and Δt is fixed at 1 hr Figure 2b shows $\mathbf{v}_{i\to j}$ averaged over all js for each i-th bin, denoted later by a forward transition, with the sample density distribution shaded underneath. The resulting transition vectors, regardless of where they originate from, have a tendency of pointing to a certain spot in the plane or hereafter called the settling point, situated in the middle of the MH regime. The settling point finds itself around $LP \sim 700$ W m^{-2} and ACRE$\sim$75 W m^{-2}, where the zero contours of the x component of transition vectors (dashed) and of its y component (dotted) intersect each other.

The convergence of transition vectors toward a settling point, although seemingly unintuitive, is physically explained as follows. To facilitate the interpretation, transition vectors are decomposed into the individual components of P and ACRE. The P growth rate, or $P^{-1}(dP/dt)$, plotted in Figure 2c implies a rapid invigoration of convection in the BH regime. The BH-regime area expands upward in P-ACRE space, suggesting that more high clouds imposing a greater ACRE have the potential to aid the deepening of convection as demonstrated by Masunaga and Bony (2018). The P growth rate is negative in a major portion, if not to the entirety as discussed below, of the TH regime. These are consistent with the theoretical expectation that an unstable growth (dissipation) of convection would occur when moisture and MSE are both imported into (exported out of) the atmospheric column (Figure 1).

The zero contour (or neutrality in P growth) runs through the MH regime, with the exception of a lower portion of it cutting into near the left end of the TH regime, which implies that precipitation can grow rather than decay even in the TH regime. It is inferred that moisture is in reality imported to sustain precipitation in this particular domain in contradiction to the original definition of the TH regime. This inconsistency arises from a limitation in the two-mode assumption in the present formulation. Past observations have revealed that the tropical vertical motion profiles outside convectively active spells can be bimodal with one weakly- ascending peak near the tropopause and the other in the lower troposphere (Gage et al., 1991; Masunaga & L'Ecuyer, 2014). The lower peak implies a low-level ascent that brings in moisture, while the upper peak bears a resemblance to a top-heavy ω structure. The two-mode model in the current formulation is unable to adequately represent such a bimodal ω profile.

ACRE on the tropical atmosphere is controlled mainly by the longwave heating of high clouds (e.g., Slingo & Slingo, 1988). ACRE is thus typically positive for tropical rainfall except in minor occasions where shallow, lightly raining clouds unaccompanied by overlapping upper-level clouds produce a slightly negative ACRE. It is confirmed with the CERES SYN1deg data set (not shown) that high cloud fraction varies monotonically with ACRE from near zero for ACRE ~ 0 to almost 100% as ACRE approaches 150 W m^{-2}. The local temporal tendency of high cloud fraction, acquired from the CERES SYN1deg data, is projected onto the P-ACRE plane in Figure 2d. High clouds tend to increase in the bottom half of the plot encompassing the TH regime while decreasing elsewhere, closely aligned with the increasing or decreasing tendency in ACRE as implied by Figure 2b. The zero contour of ACRE tendency (dotted) is indeed nearly overlapped with the boundary between the warm- and cold-colored domains depicting high cloud changes. A possible mechanism letting high clouds expand in the TH regime is that a top-heavy ascent leads to a confined layer of upper-tropospheric horizontal divergence (Bony et al., 2016). To the contrary, a less top-heavy vertical motion would be less efficient in working against the disappearance of high clouds as they gradually fall or evaporate out.

21698996, 2025, 23, Downloaded from https://agupubs.onlinelibrary.wiley.com/doi/10.1029/2025JD043909 by Hirohiko Masunaga - MPI 348 Meteorology , Wiley Online Library on [01/12/2025]. See the Terms and Conditions (https://onlinelibrary.wiley.com/terms-and-conditions) on Wiley Online Library for rules of use; OA articles are governed by the applicable Creative Commons License

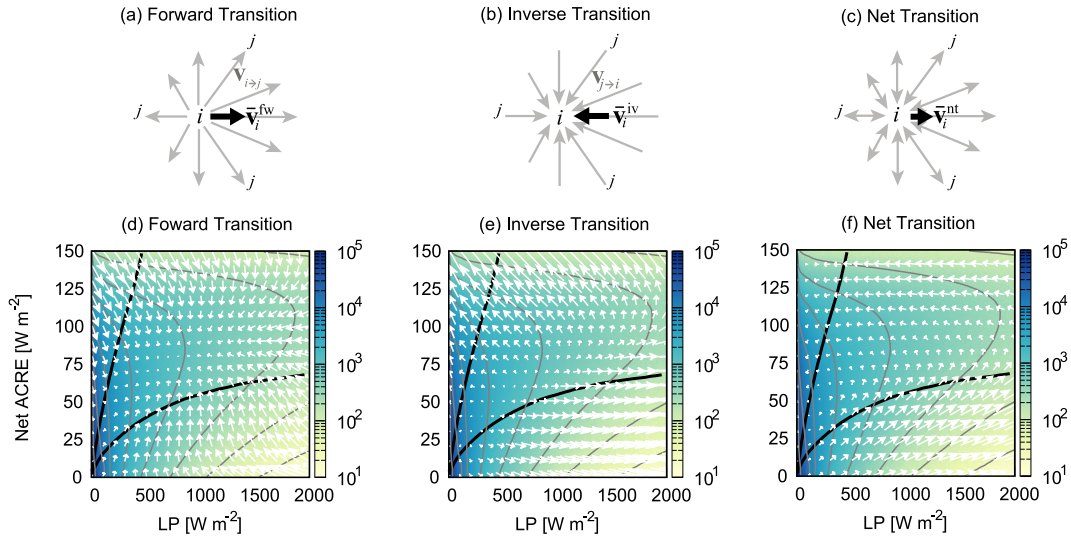

Figure 3. (a)–(c) Schematic illustration of instantaneous transition vectors (in gray) and their mean (in black) for forward transitions in (a), for inverse transitions in (b), and for net transitions in (c). (d)–(f) Transition vectors in the *P*-ACRE plane with sample density (color shade and contours) for forward transitions in (d), for inverse transitions in (e), and for net transitions in (f). Vector length implies the hourly interval of transition. The contour levels are 10, 30, 100, 300, 1,000, 3,000, and ⋯, from right to left.

4. Forward and Inverse Transitions

P and ACRE are found to rapidly evolve toward a settling point in Figure 2b. A consequence naively predicted from this is a striking sample density peak that would be sharpening increasingly with time at the settling point, which is in reality absent in Figure 2b. It will be argued below that such an unrealistic distortion of the sample density distribution is prevented from occurring by inverse transitions that largely, if not entirely, counteract the forward transitions shown so far. It is reminded that the transition vectors plotted in Figure 2b, hereafter called forward transitions, are computed as

$$\begin{aligned}\overline{\mathbf{v}}_i^{\mathrm{fw}} &= \frac{n_i \sum_j \pi_{i\to j}\mathbf{v}_{i\to j}}{n_i \sum_j \pi_{i\to j}} \\ &= \sum_j \pi_{i\to j}\mathbf{v}_{i\to j}.\end{aligned} \tag{10}$$

Here, n_i is the sample density in the i-th bin and $\pi_{i\to j}$ is the normalized probability distribution of a transition from i-th to j-th bins, where

$$\sum_j \pi_{i\to j} \equiv 1. \tag{11}$$

As such, $\overline{\mathbf{v}}_i^{\mathrm{fw}}$ represents the average of outgoing transitions from a given (i-th) state (see Figure 3a), constituting why $\overline{\mathbf{v}}_i^{\mathrm{fw}}$ is termed as "forward" transition. Figure 2b above illustrates forward transition vectors, which are copied over to Figure 3d to facilitate later comparison.

In the physical context, $\pi_{i\to j}$ summarizes the physically driven effects giving rise to the specific transition (e.g., the column processes) as well as stochastic perturbations to *P* and ACRE. The stochastic transitions include the effects of, for example, transient convective systems entering and leaving the atmospheric column. Given that the stochastic component is largely averaged out in the summation over j, the physical components principally account for $\overline{\mathbf{v}}_i^{\mathrm{fw}}$ (Figure 3a).

21698996, 2025, 23, Downloaded from https://agupubs.onlinelibrary.wiley.com/doi/10.1029/2025JD043909 by Hirohiko Masunaga - MPI 348 Meteorology , Wiley Online Library on [01/12/2025]. See the Terms and Conditions (https://onlinelibrary.wiley.com/terms-and-conditions) on Wiley Online Library for rules of use; OA articles are governed by the applicable Creative Commons License

21698996, 2025, 23, Downloaded from https://agupubs.onlinelibrary.wiley.com/doi/10.1029/2025JD043909 by Hirohiko Masunaga - MPI 348 Meteorology , Wiley Online Library on [01/12/2025]. See the Terms and Conditions (https://onlinelibrary.wiley.com/terms-and-conditions) on Wiley Online Library for rules of use; OA articles are governed by the applicable Creative Commons License

An inverse transition, or the mean of incoming transitions toward the i-th state (Figure 3b), is written as

$$\overline{\mathbf{v}}_i^{\mathrm{iv}} = \frac{\sum_j n_j \pi_{j\to i} \mathbf{v}_{j\to i}}{\sum_j n_j \pi_{j\to i}}. \tag{12}$$

The forward and inverse transitions defined this way are practically equivalent to "lagging" and "leading" evolutions, respectively, considered by Wolding et al. (2020) for studying convective development in moisture-precipitation space, although their target was slower processes than ours by choosing $\Delta t = 6$ hr instead of 1 hr.

The inverse transition field $\overline{\mathbf{v}}^{\mathrm{iv}}$, plotted in Figure 3e, illustrates a pattern very different from $\overline{\mathbf{v}}^{\mathrm{fw}}$ (Figure 3d). Forward and inverse transition vectors are pointed in nearly opposite directions in the BH and MH regimes, whereas inverse transitions are oriented in a more perpendicular direction to forward transitions in the TH regime. This difference arises in part from an inhomogeneous distribution of sample density. Unlike a forward transition being a function only of $\pi_{i\to j}$ for a given pair of i and j (Equation 10), an inverse transition depends on the sample density distribution (n_j) as well (Equation 12). When a pair of instantaneous transitions $\mathbf{v}_{j\to i}$ occur in opposite directions (i.e., two gray vectors pointing to each other in Figure 3b), they occur across a gradient of sample density; the one from densely to sparsely populated states would be given a greater weight than the other when averaged together, unless the gradient in $\pi_{j\to i}$ happens to be more than counteracting against the population gradient in Equation 12. This explains why $\overline{\mathbf{v}}^{\mathrm{iv}}$ (Figure 3e) tends to veer to down gradient across sample density contours compared to $\overline{\mathbf{v}}^{\mathrm{fw}}$ (Figure 3d). As such, inverse transitions differ in nature from forward transitions in that inverse transitions arise to a large extent from stochastic processes having an effect of smoothing the sample density distribution.

The sum of forward and inverse transition vectors defines a net transition vector,

$$\overline{\mathbf{v}}^{\mathrm{nt}} = \overline{\mathbf{v}}^{\mathrm{iv}} + \overline{\mathbf{v}}^{\mathrm{fw}}. \tag{13}$$

In areas where $\overline{\mathbf{v}}^{\mathrm{fw}}$ and $\overline{\mathbf{v}}^{\mathrm{iv}}$ point in opposite directions as mentioned above, they largely cancel each other out into a near-zero $\overline{\mathbf{v}}^{\mathrm{nt}}$. This offers a generalized version of the "dynamic equilibrium" picture discussed by MT24. If incoming and outgoing processes are nearly in balance at the i-th state, that is,

$$\sum_j n_i \pi_{i\to j} \approx \sum_j n_j \pi_{j\to i}, \tag{14}$$

Equations 10, 12 and 14 are combined into

$$\begin{aligned} \overline{\mathbf{v}}^{\mathrm{nt}} &\approx \frac{\sum_j \left(n_i \pi_{i\to j} - n_j \pi_{j\to i}\right) \mathbf{v}_{i\to j}}{n_i} \\ &\approx 0. \end{aligned} \tag{15}$$

Such a near-equilibrium state is observed generally in the BH and MH regimes (Figure 3f). Net transitions do not vanish in general in the TH regime, but imbalances occur only where sample densities are lower by orders of magnitude than elsewhere (e.g., in the lower right corner of Figure 3f). It follows that the contribution of these off-equilibrium transitions to the whole statistics is limited.

The net transition vectors as a whole overall make a counterclockwise turn in the P-ACRE space (Figure 3f). The resulting trajectory is interpreted as an initial enhancement and a subsequent decline of P accompanied by a consistent increase of ACRE. This qualitatively matches the system mean Lagrangian life cycle of convection as shown next.

5. Dynamic Equilibrium and Convective Life Cycle

The transition vectors presented above are hourly changes of P and ACRE on a spatially fixed $1^\circ \times 1^\circ$ grid. As such, the transition vectors are an Eulerian measure of short-term (~1 hr) convective variability on a hundred-kilometer scale. This choice of temporal and spatial scales justifies the Eulerian frame, since the displacement

21698996, 2025, 23, Downloaded from https://agupubs.onlinelibrary.wiley.com/doi/10.1029/2025JD043909 by Hirohiko Masunaga - MPI 348 Meteorology , Wiley Online Library on [01/12/2025]. See the Terms and Conditions (https://onlinelibrary.wiley.com/terms-and-conditions) on Wiley Online Library for rules of use; OA articles are governed by the applicable Creative Commons License

speed of cloud systems is rarely as high as 1°/h or ∼30 m s^{-1} (Feng et al., 2021; Heikenfeld et al., 2019). While isolated cumuli may be too small and too transient to be captured, well-organized convective systems could be far more long-lived and horizontally extensive than describable by a single transition vector. It follows that various grid-by-grid transitions would simultaneously occur in different places within an organized system, which as a whole would evolve with time over a system's life cycle. This motivates us to explore the physical connection between the internal transitions embedded in a convective system and the macroscopic picture of the system-wide evolution.

The Eulerian frame is no longer valid for chasing moving cloud systems over an extended period of time. Many tools and data sets have been developed to track the Lagrangian convective life cycle in satellite observations (Feng et al., 2021, 2023; Fiolleau & Roca, 2013a, 2013b; Heikenfeld et al., 2019; Takahashi et al., 2021). In the analysis that follows, evolving precipitation systems are identified by the IMERG-Convective Tracking (CT) data set (Takahashi et al., 2021). Whereas the IMERG-CT defines a precipitation system as a contiguous area with $P \geq 0.5$ mm h^{-1}, a somewhat larger rectangular domain encompassing this system is searched for precipitating grid boxes in the manner described by Masunaga and Takahashi (2024) so as to include anvil clouds extending beyond the tracked system edges.

First shown is a case study with an evolving convective system to illustrate the internal variability of convective regimes as an example. The case study is followed by a statistical analysis of all the convective events averaged.

5.1. Case Study

Figure 4 shows a sequence of snapshots depicting the evolution of a central Pacific precipitation system that lasted for 24 hr from 00 UTC on 31 May 2007 until the end of that day. This particular system was chosen arbitrarily from long-lived events over open ocean recorded in the IMERG-CT database. The longevity and oceanic conditions ensure a well-defined convective life cycle undisturbed by the complicated surface effects due to orography and overwhelming diurnal forcing.

The left column illustrates the system's life cycle at every 3 hours in the native IMERG resolution of 0.1 square degrees. The precipitation system grows over time in size and intensity until the midstage of the life cycle and then gradually shrinks toward the end. The rise and fall of precipitation is reminiscent of the net-transition trajectories found in the previous section and is also overall in line with the typical evolutionary path as known in the literature (e.g., Elsaesser et al., 2022; Fiolleau & Roca, 2013a; Futyan & Del Genio, 2007; Machado et al., 1998; Takahashi et al., 2021). A sudden expansion of the precipitating area at 9 hr likely results from a merger with a neighboring system as will become clearer later.

Instantaneous P and ACRE measurements are employed to separate the BH, MH, and TH regimes on a $1° \times 1°$ grid as shown in the right column. Each snapshot has an internal structure composed of multiple regimes in a nearly random pattern, which changes from one lifestage to another with little sign of systematic evolution. The randomness in Figure 4 offers an example visualizing the "dynamic equilibrium" discussed earlier, rather than a monotonic evolution with increasing ω top-heaviness as might be naively expected.

A short-term, small-scale variability embedded in the system, however, may not be so random. Figure 4 (right) shows such examples with two grid pixels in each of which the BH regime transitions to the MH and then to the TH (labeled by "B," "M," and "T", respectively) at an interval of 3 hours. Precipitation notably intensifies at each location where the BH regime gives way to the MH regime, as seen in the corresponding maps in the left column. These particular examples will be revisited for further discussion in Section 6.

ACRE in the same snapshots is plotted in the left column of Figure 5. A merger of two neighboring systems that occurs from 9 to 12 hr is now visually evident. The second system is tagged as a separate system in the IMERG-CT database until it is merged and is hence missing from Figure 4 above. The convective regimes are depicted again in the right column of Figure 5 but this time are drawn throughout the whole domain regardless of whether these are inside or outside the tracked system except where rainfall is absent. While the pattern is overall a random patch of different regimes, one might notice that the BH regime spreads increasingly over time as the TH regime fades away toward the end of life cycle. This qualitatively corroborates the evolution suggested by net-transition vectors, moving away from the TH regime and arriving eventually in the BH regime (Figure 3f). The growth of the BH-regime occurrence results from a domain-wide increase of ACRE evident at 21 hr, likely due to the

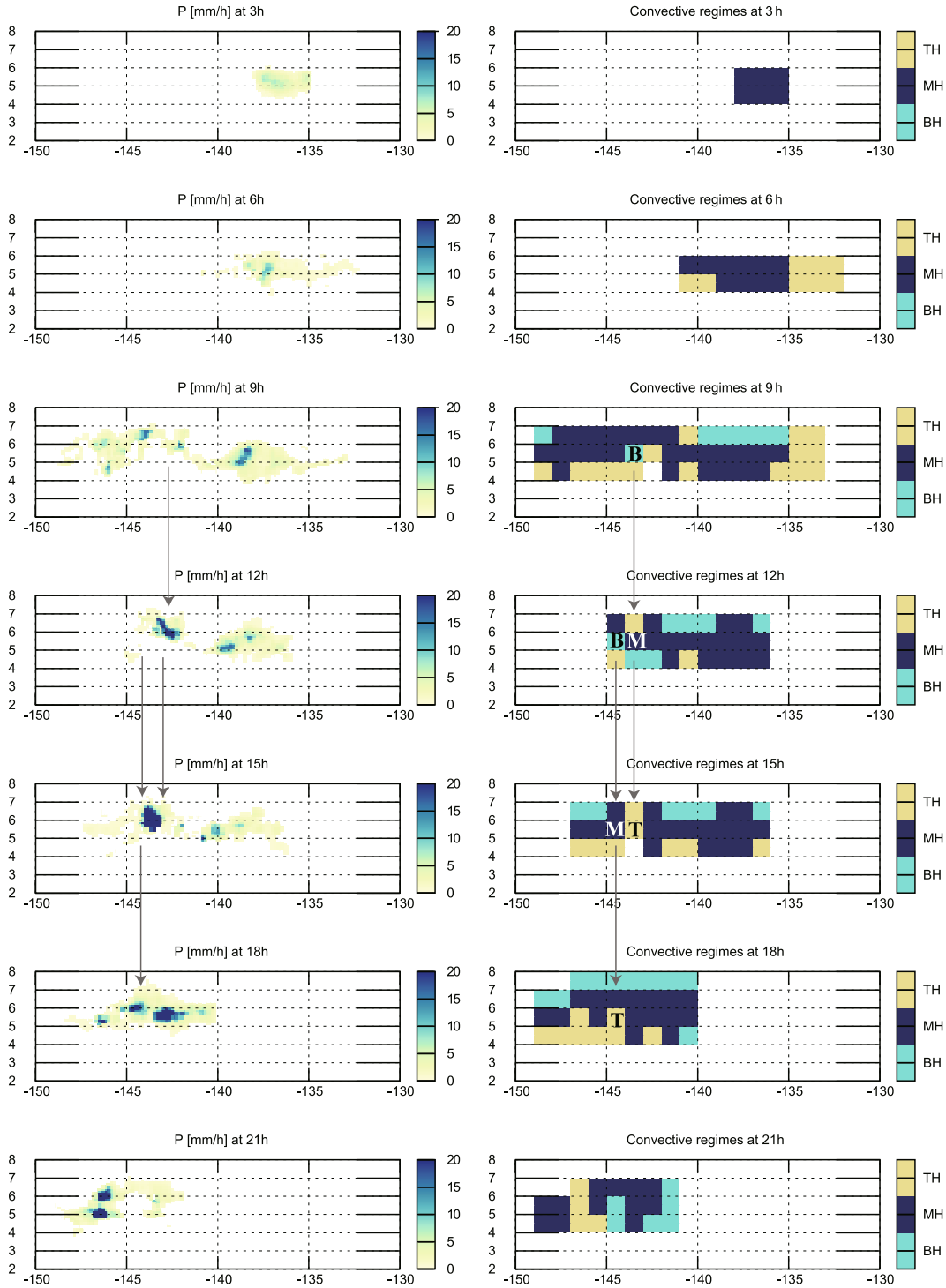

Figure 4. Sequential longitude-latitude maps delineating the evolution of a precipitation system from the IMERG-CT database at selected lifestages of 3, 6, 9, 12, 15, 18, and 21 hr from top to bottom. The precipitation rate (mm h^{-1}) is plotted in the left column and the convective regimes (BH, MH, and TH regimes) in the right. The labels "B," "M," and "T" denote the BH, MH, and TH regimes, respectively (see text for detail).

spreading of anvil clouds concurrent with a weakening of precipitation. A combination of anvil-induced long-wave heating and shallow convection beneath has the potential of reinvigorating convective activity through the unstable dynamics inherent in the BH regime (Masunaga & Bony, 2018).

21698996, 2025, 23, Downloaded from https://agupubs.onlinelibrary.wiley.com/doi/10.1029/2025JD043909 by Hirohiko Masunaga - MPI 348 Meteorology , Wiley Online Library on [01/12/2025]. See the Terms and Conditions (https://onlinelibrary.wiley.com/terms-and-conditions) on Wiley Online Library for rules of use; OA articles are governed by the applicable Creative Commons License

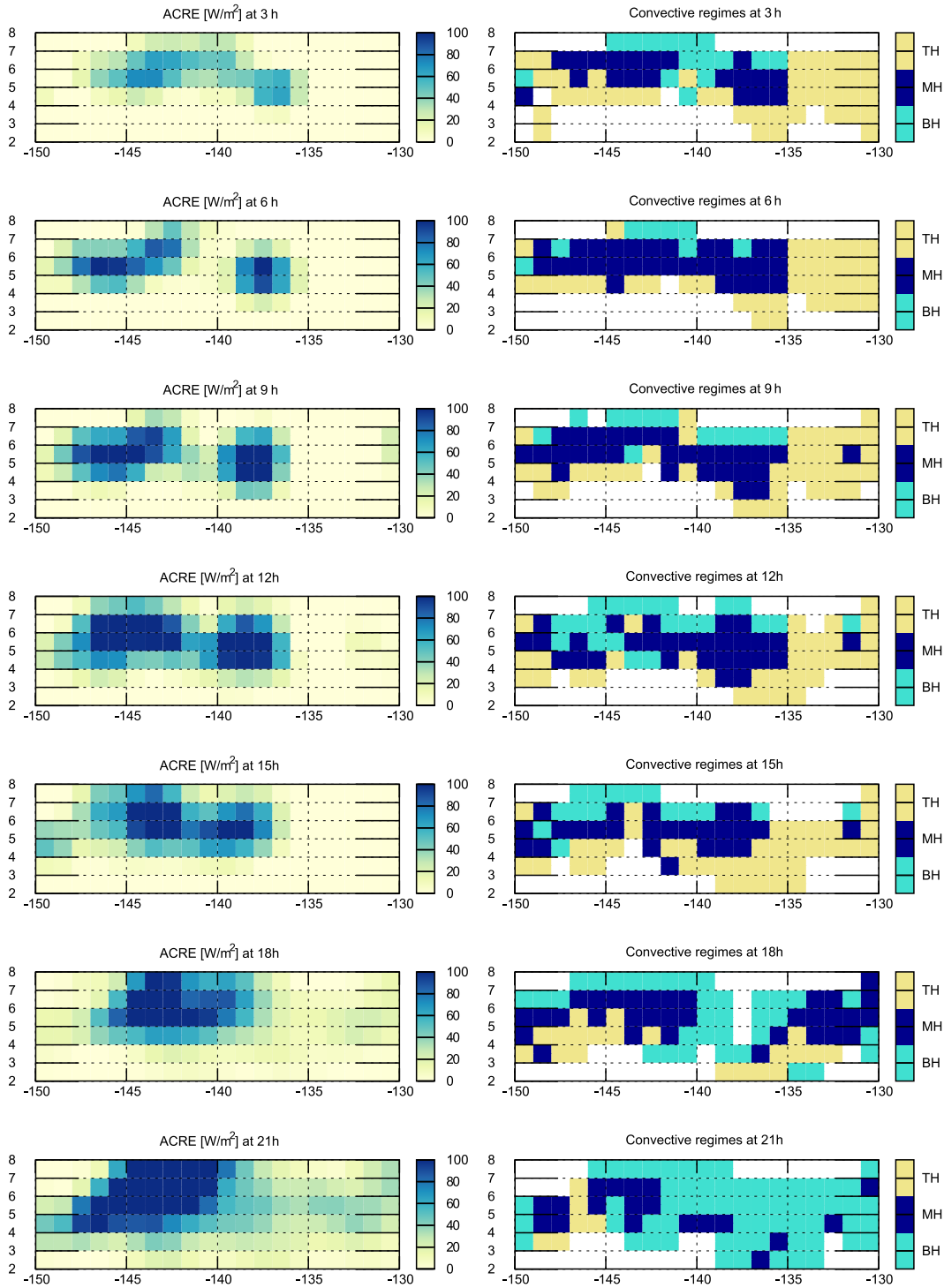

Figure 5. As Figure 4 but for atmospheric cloud radiative effect (left) and the convective regimes (right). Unlike Figure 4, the whole domain is drawn regardless of inside or outside the tracked precipitation system, exclusive of nonraining grid boxes in the right column.

21698996, 2025, 23, Downloaded from https://agupubs.onlinelibrary.wiley.com/doi/10.1029/2025JD043909 by Hirohiko Masunaga - MPI 348 Meteorology , Wiley Online Library on [01/12/2025]. See the Terms and Conditions (https://onlinelibrary.wiley.com/terms-and-conditions) on Wiley Online Library for rules of use; OA articles are governed by the applicable Creative Commons License

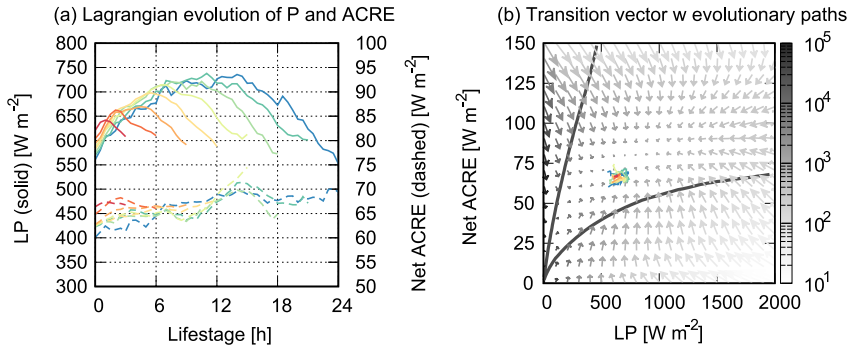

Figure 6. (a) The evolution of system-averaged *P* (solid, labeled on the left) and atmospheric cloud radiative effect (dashed, labeled on the right) over the convective life cycle for different lifetimes (shown in different colors), adapted from MT24. (b) The evolutionary trajectories from (a) projected on the *P*-ACRE plane, superimposed by forward transition vectors with the contrast adjusted to sampling density).

A case study as examined here is a useful exercise but is not statistically robust. Next investigated are the mean properties of the convective life cycle and their relevance to the present findings.

5.2. Composite Life Cycle

All the IMERG-CT precipitation systems in the tropical band (25°S-25°N) for the two years of 2007 and 2008 are ingested into the composite life cycle presented in this section. The evolution of P and ACRE as spatially averaged over the convective system area is shown in Figure 6a (adapted from Figure 7 of MT24). Each curve represents a lifetime-sorted composite life cycle obtained from many events combined together. Precipitation follows a bell-shaped evolutionary curve regardless of lifetime, while ACRE does not exhibit any systematic variability over a lifetime except a subtle but consistent increase toward the end. Note that the evolution of individual events could deviate significantly around the composite curves, especially when the evolutionary path is complicated by splitting and merging of precipitation systems.

The whole composite evolution spans a range of 550–750 W m^{-2} for LP and 60–70 W m^{-2} for ACRE, which fall close to the settling point. As a result, the evolutionary trajectories projected onto the *P*-ACRE plane (Figure 6b) are clearly confined in the vicinity of a spot where forward transition vectors converge to.

Figure 6a shows that the system-averaged precipitation first rises and then declines as ACRE slightly increases through the lifetime. As mentioned in the end of Section 4, this pattern bears qualitative resemblance to the counterclockwise paths depicted by an ensemble of net transition vectors in Figure 3f, except that the transition vector field is spread broadly across the *P*-ACRE plane unlike the composite life cycle being confined to the near-settling point. Transition vectors by design represent the internal processes within a parent convective system (on a one-degree grid scale), while the Lagrangian life cycle illustrates the system-wide evolution, as visually exemplified in Figure 4. It follows that although the greater magnitude of variability on a smaller scale is largely averaged out when integrated into a system scale, the qualitative features in the *P*-ACRE space are mostly preserved through the averaging. This fact itself is more predictable than surprising, but it is reminded that net transition vectors emerge only after forward and inverse transitions nearly cancel each other out. It is the small residual arising nearly from the cancellation that determines the overall characteristics of the convective life cycle.

6. Discussion

6.1. Convective Life Cycle and Dynamic Equilibrium

The tendency toward a midheavy state corroborates the theoretical expectation that a state of negative NGMS would be evolved toward a stable equilibrium with positive NGMS (Raymond, 2000; Raymond et al., 2009). Such a monotonic equilibrating process, however, does not intuitively agree with the convective life cycle as we know it. Vertical motion has been confirmed in past studies (Y.-C. Chen & Masunaga, 2024; Inoue & Back, 2015a, 2015b; Masunaga & L'Ecuyer, 2014; Maithel & Back, 2022) to become increasingly top-heavy as convection

21698996, 2025, 23, Downloaded from https://agupubs.onlinelibrary.wiley.com/doi/10.1029/2025JD043909 by Hirohiko Masunaga - MPI 348 Meteorology , Wiley Online Library on [01/12/2025]. See the Terms and Conditions (https://onlinelibrary.wiley.com/terms-and-conditions) on Wiley Online Library for rules of use; OA articles are governed by the applicable Creative Commons License

develops deeper and eventually dies out. As a result, NGMS would change its sign from negative (bottom-heavy) to positive (mid-heavy) and eventually back to negative (top-heavy). This contrasts with the proneness to settle into a state of positive NGMS as implied in this study.

Potential causes for the apparent inconsistencies between the present (and MT24's) findings and convectional knowledge are discussed from three different angles.

6.1.1. Vertical Motion Estimates

Vertical motion of the atmosphere (ω) is difficult to measure. Different reanalysis data sets often disagree with one another in the vertical structure of ω even qualitatively (Huaman et al., 2021). In situ sounding arrays deployed for field campaign programs offer another source of vertical velocity estimates independent of reanalysis data at the expense of the limited availability of observations in both space and time. Nonetheless, the one-way evolution from bottom-heavy to top-heavy ω profiles over the convective life cycle has been consistently confirmed regardless of methodology, that is, from the sounding array (Figure 3 of Inoue and Back (2015a), Figure 9a of Inoue and Back (2015b), and Figure 10 of Maithel and Back (2022)) and ERA5 data (Figure 4 of Y.-C. Chen and Masunaga (2024)).

The three convective regimes having different degrees of ω top-heaviness are separated in this work from satellite-observed precipitation and ACRE. The present approach uses neither in situ nor reanalysis-provided ω but instead relies on the semianalytic model forced by satellite observables in which vertical motion is extracted from the vertical moisture advection term (Equations 5 and 6). A practically identical approach was tested earlier by Masunaga and L'Ecuyer (2014) to illustrate the temporal change in ω. Their result confirms the monotonic evolution of ω toward top-heavy structure is closely in line with the previously known convective life cycle but seemingly at odds with the present conclusion.

What, then, led to the contradicting pictures regarding how the ω top-heaviness evolves? A potential cause lies in whether an Eulerian or Lagrangian framework is chosen when defining a convective life cycle, as discussed next.

6.1.2. Eulerian Versus Lagrangian

The temporal evolution of ω was investigated by previous studies (Y.-C. Chen & Masunaga, 2024; Inoue & Back, 2015b; Masunaga & L'Ecuyer, 2014; Maithel & Back, 2022), in which the evolution was defined in a spatially fixed coordinate system. Such an Eulerian convective life cycle consists only of the convective system samples that occur within the study domain, which could be qualitatively different from a Lagrangian life cycle of a traveling cloud system throughout its lifetime.

A clue to reconcile the contradicting evolutionary scenarios was already found in Section 5.1. A transition from the BH to MH and then to the TH regimes is observed momentarily at a fixed location within the precipitation system, although such a one-way evolution is hardly recognized over the life cycle of the parent system (Figure 4). An analogous example may be found in a moving squall line consisting of convective cells at the front of the system, accompanied by a trailing stratiform anvil on its rear (e.g., Zipser, 1977). The stratiform anvil would lag the convective cells when observed in the Eulerian framework as the convective system marches in and out of the study domain. From the Lagrangian point of view, on the other hand, the convective cells and stratiform anvil would coexist without any appreciable time lag over an extended period of time. Similar interpretation may be applied to explain how the vertical structure of ω would look like when projected onto the Eulerian or Lagrangian coordinates.

A more technical (but potentially important) difference between Eulerian and Lagrangian analyses could arise from a methodological limitation of Lagrangian tracking. Precipitation rates lower than 0.5 mm h^{-1} on a 0.1° grid scale are excluded when defining precipitation systems in the data set used by MT24 (Takahashi et al., 2021), ensuring the robust performance of the tracking algorithm. In contrast, infrared-based tracking algorithms define system boundaries more conservatively, focusing solely on cold cloud shields that radiometrically contrast with surface emissions. As such, Lagrangian tracking is by design applicable only when the target convective system has grown to a certain degree, in contrast with the Eulerian frame in which the transition from convectively inactive to active spells or vice versa can be captured to its entirety.

21698996, 2025, 23, Downloaded from https://agupubs.onlinelibrary.wiley.com/doi/10.1029/2025JD043909 by Hirohiko Masunaga - MPI 348 Meteorology , Wiley Online Library on [01/12/2025]. See the Terms and Conditions (https://onlinelibrary.wiley.com/terms-and-conditions) on Wiley Online Library for rules of use; OA articles are governed by the applicable Creative Commons License

21698996, 2025, 23, Downloaded from https://agupubs.onlinelibrary.wiley.com/doi/10.1029/2025JD043909 by Hirohiko Masunaga - MPI 348 Meteorology , Wiley Online Library on [01/12/2025]. See the Terms and Conditions (https://onlinelibrary.wiley.com/terms-and-conditions) on Wiley Online Library for rules of use; OA articles are governed by the applicable Creative Commons License

It is noted that while individual cumulus cells rarely live for much longer than an hour, a sequence of multiple cells could produce a long-lived convective system if one cell successfully keeps triggering next cells. In other words, an organized convective system is incessantly "metabolized" even if the system as a whole does not exhibit much morphological change over time. This points to another key issue to discuss, that is, the temporal scale of the regime-to-regime transitions and its connection to the evolution of the whole convective system.

6.1.3. Transition Time Scale and Dynamic Equilibrium

The bottom- to top-heavy evolution of ω over the convective life cycle as found in previous work often has a time scale of 24 hr or even longer (Y.-C. Chen & Masunaga, 2024; Inoue & Back, 2015a; Masunaga & L'Ecuyer, 2014). This is substantially longer than the hourly time scale typical of the transitions in the P-ACRE space (it is reminded that each vector depicts a change over 1 hour in Figure 3). The transition from one convective regime to another, driven by the rapid equilibrating tendency from an unstable state of negative NGMS (BH and TH regimes) to a stable equilibrium with positive NGMS (MH regime) (Raymond, 2000), is thus more likely interpreted as part of the metabolizing processes rather than a measure of the evolution as a system. The near immobility of the composite life cycle trajectories in the P-ACRE space in Figure 6 suggests that the equilibration by the mutually competing (forward and inverse) transitions should be so rapid that every lifestage of evolution almost instantly adjusts itself to a state of dynamic equilibrium. As discussed in Section 7, dynamic equilibrium as implied from the current analysis is achieved by imperfect equilibration between the opposite transitions, and a small departure from equilibrium accounts for the qualitative nature of a convective life cycle. Such a quasi-homeostatic mechanism might be part of the mechanism that sustains a convective system over a prolonged lifetime from time to time.

6.2. The Settling Point

It remains unanswered why the settling point should have the particular values they have. A steady-state ($D_t \equiv 0$) version of Equations 1 and 2 lead to

$$\gamma = -\frac{\langle \omega \partial_t h \rangle'}{L \langle \omega \partial_t q \rangle'} \approx \frac{\langle Q_R \rangle'}{LP}, \tag{16}$$

where γ is the (nonmode-decomposed) normalized GMS. For the settling point of LP $\sim$ 700 W m^{-2} and ACRE $\sim$ 75 W m^{-2}, γ is found to be $\sim$0.11. Stephens et al. (2024) found a statistical correlation between P and ACRE with a regressed slope of 4.96 W m^{-2}/(mm d^{-1}), which is equivalent to $\gamma \sim 0.17$, a value close to the current estimate despite a vast difference in analysis strategy. The average rate at which ACRE increases with LP flattens once LP exceeds 250–500 m^{-2} (X. Chen et al., 2025). This turning point happens to be close to the settling point, although the physical processes behind this are unknown.

The observational evidence that the tropical atmosphere appears to prefer a γ of 0.1–0.2 is, although the reasons are not obvious, potentially useful for a conceptual model of tropical convection or even for more complex numerical models as an ingredient of subgrid-scale parameterization schemes.

7. Concluding Remarks

In this work, satellite-retrieved precipitation and radiation measurements were analyzed for observationally identifying the thermodynamic processes induced by vertical motion. A simple diagnostic model developed in a previous study (MT24) is employed to quantify the column processes varying with degrees of skewness in the vertical distribution of ω, namely BH, MH, and TH regimes, as a function of P and ACRE. This enables to differentiate the three convective regimes with satellite observables without direct knowledge of ω itself.

The temporal tendency of P and ACRE defines transitions between different thermodynamic states having contrasting degrees of top-heaviness. The most striking feature found in the present analysis is that forward transition vectors have a tendency of converging toward a settling point at LP $\sim$ 700 W m^{-2} and ACRE $\sim$ 75 W m^{-2}. This behavior turns out to overall meet theoretical expectations such as an unstable growth of

21698996, 2025, 23, Downloaded from https://agupubs.onlinelibrary.wiley.com/doi/10.1029/2025JD043909 by Hirohiko Masunaga - MPI 348 Meteorology , Wiley Online Library on [01/12/2025]. See the Terms and Conditions (https://onlinelibrary.wiley.com/terms-and-conditions) on Wiley Online Library for rules of use; OA articles are governed by the applicable Creative Commons License

convection in the BH regime and a convective dissipation in the TH regime. The physically driven forward transitions are counteracted by inverse transitions attributed more to a sample density gradient across the states. The forward and inverse transitions are largely balanced against each other in the BH and MH regimes, indicative of a state of dynamic equilibrium as argued by MT24. An equilibrium is generally not expected to be achieved in the TH regime, although the off-equilibrium states occur infrequently.

It is however important to note that the cancellation between forward and inverse transitions is incomplete, leaving behind a small but non-negligible residual. This net transition is indicative of a counterclockwise trajectory in P-ACRE space, qualitatively reminiscent of the Lagrangian life cycle of a moving convective system. When averaged spatially over the whole system, P and ACRE stay in the close vicinity of the settling point over their life cycles. It is presumed from this result that the equilibrating processes, and disequilibrating ones working against perfect equilibration, may play an essential role in the internal dynamics of Lagrangian-tracked convective systems. This supports MT24's conclusion that each lifestage quickly adjusts itself to a state of dynamic equilibrium among different degrees of the ω top-heaviness rather than following a one-way path from bottom-heavy to top-heavy states.

The findings above suggest some previously unexplored aspects of tropical convective dynamics. The tendency toward an MH state meets a theoretical expectation of NGMS thinking (Raymond, 2000), which is however not precisely in line with the convective life cycle as we know it. A solution to reconcile the apparent inconsistency lies in the dynamic equilibrium hypothesis that physically driven forward transitions are nearly balanced against statistically explained inverse transitions, with a small disequilibrium in between accounting for convective life cycles. The present analysis with satellite measurements supports this hypothesis at least to a certain degree. Future work is being planned to verify this idea with a variety of data sources including numerical model simulations and field campaign observations.

Conflict of Interest

The authors declare no conflicts of interest relevant to this study.

Data Availability Statement

The IMERG precipitation data are provided by Goddard Earth Sciences Data and Information Services Center (GES DISC) (https://doi.org/10.5067/GPM/IMERG/3B-HH/07) (Huffman et al., 2023). The CERES SYN1deg radiation product is available from NASA Langley Atmospheric Science Data Center (https://doi.org/10.5067/TERRA + AQUA/CERES/SYN1DEG-1HOUR_L3.004A) (NASA/LARC/SD/ASDC, 2017). The ERA5 CWV data are provided by Copernicus Climate Change Service (C3S) Climate Data Store (CDS) (https://doi.org/10.24381/cds.adbb2d47) (Hersbach et al., 2023). The method and availability of the IMERG-CT data set are as described by Takahashi et al. (2021). All the results presented in this paper can be reproduced with these data.

Acknowledgments
The authors are grateful to Johnny Luo, Claudia Stubenrauch, and anonymous reviewers for their comments and insights. HM was supported by the Japan Science and Technology Agency (JST) Moonshot R&D Program JPMJMS2389. HT was supported by NASA Grant 80NSSC20K0090, and part of this work was performed at the Jet Propulsion Laboratory, California Institute of Technology, under a contract with the National Aeronautics and Space Administration (80NM0018D0004).

References

Back, L. E., & Bretherton, C. S. (2009). On the relationship between SST gradients, boundary layer winds, and convergence over the tropical oceans. *Journal of Climate*, *22*(15), 4187–4196. https://doi.org/10.1175/2009JCLI2392.1

Back, L. E., Hansen, Z., & Handlos, Z. (2017). Estimating vertical motion profile top-heaviness: Reanalysis compared to satellite-based observations and stratiform rain fraction. *Journal of the Atmospheric Sciences*, *74*(3), 855–864. https://doi.org/10.1175/JAS-D-16-0062.1

Bony, S., Stevens, B., Coppin, D., Becker, T., Reed, K. A., Voigt, A., & Medeiros, B. (2016). Thermodynamic control of anvil cloud amount. *Proceedings of the National Academy of Sciences*, *113*(32), 8927–8932. https://doi.org/10.1073/pnas.1601472113

Bretherton, C. S., Peters, M. E., & Back, L. E. (2004). Relationships between water vapor path and precipitation over the tropical oceans. *Journal of Climate*, *17*(7), 1517–1528. https://doi.org/10.1175/1520-0442(2004)017<1517:rbwvpa>2.0.co;2

Charney, J. G. (1963). A note on large-scale motions in the tropics. *Journal of the Atmospheric Sciences*, *20*(6), 607–609. https://doi.org/10.1175/1520-0469(1963)020<0607:anolsm>2.0.co;2

Chen, X., Stubenrauch, C. J., & Mandorli, G. (2025). Relationship between latent and radiative heating fields of tropical cloud systems using synergistic satellite observations. *Atmospheric Chemistry and Physics*, *25*(13), 6857–6880. https://doi.org/10.5194/acp-25-6857-2025

Chen, Y.-C., & Masunaga, H. (2024). The tropical convective evolution in different rain types over the west and east Pacific. *SOLA*, *20*, 392–399. https://doi.org/10.2151/sola.2024-052

Chikira, M. (2014). Eastward-propagating intraseasonal oscillation represented by Chikira-Sugiyama cumulus parameterization. Part II: Understanding moisture variation under weak temperature gradient balance. *Journal of the Atmospheric Sciences*, *71*(2), 615–639. https://doi.org/10.1175/jas-d-13-038.1

Doelling, D. R., Sun, M., Nguyen, L. T., Nordeen, M. L., Haney, C. O., Keyes, D. F., & Mlynczak, P. E. (2016). Advances in geostationary-derived longwave fluxes for the CERES synoptic (SYN1deg) product. *Journal of Atmospheric and Oceanic Technology*, *33*(3), 503–521. https://doi.org/10.1175/JTECH-D-15-0147.1

Elsaesser, G. S., Roca, R., Fiolleau, T., Del Genio, A. D., & Wu, J. (2022). A simple model for tropical convective cloud shield area growth and decay rates informed by geostationary IR, GPM, and Aqua/AIRS satellite data. *Journal of Geophysical Research*, *127*(10), e2021JD035599. https://doi.org/10.1029/2021JD035599

Feng, Z., Hardin, J., Barnes, H. C., Li, J., Leung, L. R., Varble, A., & Zhang, Z. (2023). PyFLEXTRKR: A flexible feature tracking python software for convective cloud analysis. *Geoscientific Model Development*, *16*(10), 2753–2776. https://doi.org/10.5194/gmd-16-2753-2023

Feng, Z., Leung, L. R., Liu, N., Wang, J., Houze Jr, R. A., Li, J., et al. (2021). A global high-resolution mesoscale convective system database using satellite-derived cloud tops, surface precipitation, and tracking. *Journal of Geophysical Research*, *126*(8), e2020JD034202. https://doi.org/10.1029/2020JD034202

Fiolleau, T., & Roca, R. (2013a). An algorithm for the detection and tracking of tropical mesoscale convective systems using infrared images from geostationary satellite. *IEEE Transactions on Geoscience and Remote Sensing*, *51*(7), 4302–4315. https://doi.org/10.1109/TGRS.2012.2227762

Fiolleau, T., & Roca, R. (2013b). Composite life cycle of tropical mesoscale convective systems from geostationary and low Earth orbit satellite observations: Method and sampling considerations. *Quarterly Journal of the Royal Meteorological Society*, *139*(673), 941–953. https://doi.org/10.1002/qj.2174

Futyan, J. M., & Del Genio, A. D. (2007). Deep convective system evolution over Africa and the tropical Atlantic. *Journal of Climate*, *20*, 5041–5060. https://doi.org/10.1175/JCLI4297.1

Gage, K. S., McAfee, J. R., Carter, D. A., Ecklund, W. L., Riddle, A. C., Reid, G. C., & Balsley, B. B. (1991). Long-term mean vertical motion over the tropical Pacific: Wind-profiling Doppler radar measurements. *Science*, *254*(5039), 1771–1773. https://doi.org/10.1126/science.254.5039.1771

Heikenfeld, M., Marinescu, P. J., Christensen, M., Watson-Parris, D., Senf, F., van den Heever, S. C., & Stier, P. (2019). Tobac 1.2: Towards a flexible framework for tracking and analysis of clouds in diverse datasets. *Geoscientific Model Development*, *12*(11), 4551–4570. https://doi.org/10.5194/gmd-12-4551-2019

Hersbach, H., Bell, B., Berrisford, P., Biavati, G., Horányi, A., Muñoz Sabater, J., et al. (2023). ERA5 hourly data on single levels from 1940 to present [dataset]. *Copernicus Climate Change Service (C3S) Climate Data Store (CDS)*. https://doi.org/10.24381/cds.adbb2d47

Hersbach, H., Bell, B., Berrisford, P., Hirahara, S., Horányi, A., Muñoz Sabater, J., et al. (2020). The ERA5 global reanalysis. *Quarterly Journal of the Royal Meteorological Society*, *146*(730), 1999–2049. https://doi.org/10.1002/qj.3803

Holloway, C. E., & Neelin, J. D. (2009). Moisture vertical structure, column water vapor, and tropical deep convection. *Journal of the Atmospheric Sciences*, *66*(6), 1665–1683. https://doi.org/10.1175/2008jas2806.1

Huaman, L., Schumacher, C., & Sobel, A. H. (2021). Assessing the vertical velocity of the east Pacific ITCZ. *Geophysical Research Letters*, *49*(1), e2021GL096192. https://doi.org/10.1029/2021GL096192

Huffman, G. J., Bolvin, D. T., Braithwaite, D., Hsu, K.-L., Joyce, R. J., Kidd, C., et al. (2020). Integrated multi-satellite retrievals for the global precipitation measurement (GPM) mission (IMERG). In V. Levizzani, C. Kidd, D. B. Kirschbaum, C. D. Kummerow, K. Nakamura, & F. J. Turk (Eds.), *Satellite precipitation measurement* (Vol. 1, pp. 343–353). Springer International Publishing. https://doi.org/10.1007/978-3-030-24568-9_19

Huffman, G. J., Stocker, E. F., Bolvin, D. T., Nelkin, E. J., & Tan, J. (2023). GPM IMERG final precipitation L3 half hourly 0.1 degree x 0.1 degree V07 [dataset]. *Goddard Earth Sciences Data and Information Services Center (GES DISC)*. https://doi.org/10.5067/GPM/IMERG/3B-HH/07

Igel, M. R. (2017). The tropical precipitation pickup threshold and clouds in a radiative convective equilibrium model: II. Two-layer moisture. *Journal of Geophysical Research*, *122*(12), 6469–6487. https://doi.org/10.1002/2016JD025908

Inoue, K., Adames, A. F., & Yasunaga, K. (2020). Vertical velocity profiles in convectively coupled equatorial waves and mjo: New diagnoses of vertical velocity profiles in the wavenumber-frequency domain. *Journal of the Atmospheric Sciences*, *77*(6), 2139–2162. https://doi.org/10.1175/JAS-D-19-0209.1

Inoue, K., & Back, L. E. (2015). Column-integrated moist static energy budget analysis on various time scales during TOGA COARE. *Journal of the Atmospheric Sciences*, *72*(5), 1856–1870. https://doi.org/10.1175/jas-d-14-0249.1

Inoue, K., & Back, L. E. (2015). Gross moist stability assessment during TOGA COARE: Various interpretations of gross moist stability. *Journal of the Atmospheric Sciences*, *72*(11), 4148–4166. https://doi.org/10.1175/jas-d-15-0092.1

Inoue, K., & Back, L. E. (2017). Gross moist stability analysis: Assessment of satellite-based products in the GMS plane. *Journal of the Atmospheric Sciences*, *74*(6), 1819–1837. https://doi.org/10.1175/JAS-D-16-0218.1

Inoue, K., Biasutti, M., & Fridlind, A. M. (2021). Evidence that horizontal moisture advection regulates the ubiquitous amplification of rainfall variability over tropical oceans. *Journal of the Atmospheric Sciences*, *78*(2), 529–547. https://doi.org/10.1175/JAS-D-20-0201.1

Kuang, Z. (2011). The wavelength dependence of the gross moist stability and the scale selection in the instability of column-integrated moist static energy. *Journal of the Atmospheric Sciences*, *68*(1), 61–74. https://doi.org/10.1175/2010jas3591.1

Machado, L. A. T., Rossow, W. B., Guedes, R. L., & Walker, A. W. (1998). Life cycle variations of mesoscale convective systems over the Americas. *Monthly Weather Review*, *126*(6), 1630–1654. https://doi.org/10.1175/1520-0493(1998)126<1630:lcvomc>2.0.co;2

Maithel, V., & Back, L. (2022). Moisture recharge-discharge cycles: A gross moist stability-based phase angle perspective. *Journal of the Atmospheric Sciences*, *79*(9), 2401–2417. https://doi.org/10.1175/JAS-D-21-0297.1

Mapes, B., Tulich, S., Lin, J., & Zuidema, P. (2006). The mesoscale convection life cycle: Building block or prototype for large-scale tropical waves? *Dynamics of Atmospheres and Oceans*, *42*(1–4), 3–29. https://doi.org/10.1016/j.dynatmoce.2006.03.003

Masunaga, H. (2013). A satellite study of tropical moist convection and environmental variability: A moisture and thermal budget analysis. *Journal of the Atmospheric Sciences*, *70*(8), 2443–2466. https://doi.org/10.1175/jas-d-12-0273.1

Masunaga, H. (2023). The edge intensification of Eastern Pacific ITCZ convection. *Journal of Climate*, *36*(10), 3469–3480. https://doi.org/10.1175/JCLI-D-22-0382.1

Masunaga, H., & Bony, S. (2018). Radiative invigoration of tropical convection by preceding cirrus clouds. *Journal of the Atmospheric Sciences*, *75*, 1327–1342. https://doi.org/10.1002/2016MS000855

Masunaga, H., & L'Ecuyer, T. S. (2014). A mechanism of tropical convection inferred from observed variability in the moist static energy budget. *Journal of the Atmospheric Sciences*, *71*, 3747–3766.

Masunaga, H., & Mapes, B. E. (2020). A mechanism for the maintenance of sharp tropical margins. *Journal of the Atmospheric Sciences*, *77*(4), 1181–1197. https://doi.org/10.1175/JAS-D-19-0154.1

Masunaga, H., & Sumi, Y. (2017). A toy model of tropical convection with a moisture storage closure. *Journal of Advances in Modeling Earth Systems*, *9*(1), 647–667. https://doi.org/10.1002/2016MS000855

Masunaga, H., & Takahashi, H. (2024). The energetics of the Lagrangian evolution of tropical convective systems. *Journal of the Atmospheric Sciences*, *81*(4), 783–799. https://doi.org/10.1175/JAS-D-23-0141.1

21698996, 2025, 23, Downloaded from https://agupubs.onlinelibrary.wiley.com/doi/10.1029/2025JD043909 by Hirohiko Masunaga - MPI 348 Meteorology , Wiley Online Library on [01/12/2025]. See the Terms and Conditions (https://onlinelibrary.wiley.com/terms-and-conditions) on Wiley Online Library for rules of use; OA articles are governed by the applicable Creative Commons License

NASA/LARC/SD/ASDC. (2017). CERES and GEO-Enhanced TOA, within-atmosphere and surface fluxes, clouds and aerosols 1-hourly terra-aqua Edition4A [dataset]. *NASA Langley Atmospheric Science Data Center DAAC*. https://doi.org/10.5067/TERRA+AQUA/CERES/SYN1DEG-1HOUR_L3.004A

Raymond, D. J. (2000). Thermodynamic control on tropical rainfall. *Quarterly Journal of the Royal Meteorological Society*, *126*(564), 889–898. https://doi.org/10.1002/qj.49712656406

Raymond, D. J., Sessions, S. L., & Fuchs, Ž. (2007). A theory for the spinup of tropical depressions. *Quarterly Journal of the Royal Meteorological Society*, *133*(628), 1743–1754. https://doi.org/10.1002/qj.125

Raymond, D. J., Sessions, S. L., Sobel, A. H., & Fuchs, Ž. (2009). The mechanics of gross moist stability. *Journal of Advances in Modeling Earth Systems*, *1*(3), 9. https://doi.org/10.3894/JAMES.2009.1.9

Sherwood, S. C. (1999). Convective precursors and predictability in the tropical Western Pacific. *Monthly Weather Review*, *127*(12), 2977–2991. https://doi.org/10.1175/1520-0493(1999)127<2977:cpapit>2.0.co;2

Slingo, A., & Slingo, J. M. (1988). The response of a general circulation model to cloud longwave radiative forcing. I: Introduction and initial experiments. *Quart. J. Roy. Meteor. Soc.*, *114*(482), 1027–1062. https://doi.org/10.1002/qj.49711448209

Sobel, A. H., Nilsson, J., & Polvani, N. L. (2001). The weak temperature gradient approximation and balanced tropical moisture waves. *Journal of the Atmospheric Sciences*, *58*(23), 3650–3665. https://doi.org/10.1175/1520-0469(2001)058<3650:twtgaa>2.0.co;2

Stephens, G. L., Shiro, K. A., Hakuba, M. Z., Takahashi, H., Pilewskie, J. A., Andrews, T., et al. (2024). Tropical deep convection, cloud feedbacks and climate sensitivity. *Surveys in Geophysics*, *45*(6), 1903–1931. https://doi.org/10.1007/s10712-024-09831-1

Takahashi, H., Lebsock, M., Luo, Z. J., Masunaga, H., & Wang, C. (2021). Detection and tracking of tropical convective storms based on globally gridded precipitation measurements: Algorithm and survey over the tropics. *Journal of Applied Meteorology and Climatology*, *60*(3), 403–421. https://doi.org/10.1175/JAMC-D-20-0171.1

Wolding, B., Dias, J., Kiladis, G., Ahmed, F., Powell, S. W., Maloney, E., & Branson, M. (2020). Interactions between moisture and tropical convection. Part I: The coevolution of moisture and convection. *Journal of the Atmospheric Sciences*, *77*(5), 1783–1799. https://doi.org/10.1175/JAS-D-19-0225.1

Wolding, B., Powell, S. W., Ahmed, F., Dias, J., Gehne, M., Kiladis, G., & Neelin, J. D. (2022). Tropical thermodynamic-convection coupling in observations and reanalyses. *Journal of the Atmospheric Sciences*, *79*(7), 1781–1803. https://doi.org/10.1175/JAS-D-21-0256.1

Yoneyama, K., & Fujitani, T. (1995). The behavior of dry westerly air associated with convection observed during the TOGA-COARE R/V Natsushima cruise. *Journal of the Meteorological Society of Japan. Ser. II*, *73*(2B), 291–304. https://doi.org/10.2151/jmsj1965.73.2b_291

Zipser, E. J. (1977). Mesoscale and convective-scale downdrafts as distinct components of squall-line structure. *Monthly Weather Review*, *105*(12), 1568–1589. https://doi.org/10.1175/1520-0493(1977)105<1568:macdad>2.0.co;2

21698996, 2025, 23, Downloaded from https://agupubs.onlinelibrary.wiley.com/doi/10.1029/2025JD043909 by Hirohiko Masunaga - MPI 348 Meteorology , Wiley Online Library on [01/12/2025]. See the Terms and Conditions (https://onlinelibrary.wiley.com/terms-and-conditions) on Wiley Online Library for rules of use; OA articles are governed by the applicable Creative Commons License